Reservoir depressurization driven by passive gas emissions at Ambrym volcano

Tara Shreve, R. Grandin, Marie Boichu

Reservoir depressurization driven by passive gas emissions at Ambrym volcano

T. Shreve[a,b], R. Grandin[a], M. Boichu[c]

[a]Université de Paris, Institut de physique du globe de Paris, CNRS, F-75005, Paris, France

[b]Earth and Planets Laboratory, Carnegie Institution for Science, Washington, District of Columbia, USA

[c]Université de Lille, UMR 8518 – LOA – Laboratoire d'Optique Atmosphérique, F-59000, Lille, France

Highlights:

- Persistent volcanic degassing explains steady subsidence at Ambrym from 2015–2017
- Subsidence ends in 2017, as magma influx balances depressurization from degassing
- We estimate a magma influx of $\sim$0.16 km^3 over 14 months before the 2018 eruption

Keywords: Subsidence, Degassing processes, Magma replenishment

Corresponding author: Tara Shreve, tshreve@carnegiescience.edu

Abstract

Despite being a widespread and common process, the impact of passive volcanic degassing on the pressurization state of a magma reservoir is not well understood. If mass loss due to gas emissions results in reservoir depressurization and surface subsidence, the pressure difference between a shallow reservoir and deep magma source may result in magma recharge and eventually trigger an eruption. It is therefore important to determine how a simplified reservoir-conduit system responds to such degassing processes. Here we use an extreme example of persistent volcanic degassing—Ambrym—as a case study to relate sulphur dioxide mass flux with reservoir depressurization and edifice-scale subsidence, both measured from satellite-based remote sensing observations. A geodetic inversion of surface displacements measured with Interferometric Synthetic Aperture Radar modeled using the Boundary Element Method provides bounds on the reservoir pressure change during an episode of subsidence at Ambrym from 2015 to 2017. These results are input into a lumped parameter theoretical model developed by Girona et al. (2014), and the free parameters (e.g., reservoir size and conduit radius) are systematically explored. We find that the 2015–2017 subsidence episode is consistent with pressure decreasing at a rate of -5.2 to -2.0 MPa year^{-1} in a reservoir at $\sim$2 km b.s.l., as a result of passive degassing. The subsidence episode is observed to end abruptly in October 2017, and no significant deformation is detected in the 14 months leading up to a rift zone intrusion and submarine eruption in December 2018, despite substantial degassing. We explain this lack of pre-eruptive deformation by an influx of $\sim$0.16 km^3 of magma into a shallow ($<$ 2 km b.s.l.) reservoir that counterbalances the depressurization caused by degassing. This

recharge volume is comparable with the volume of magma subsequently extracted from Ambrym's reservoir in December 2018. We conclude that at some open-vent passively degassing volcanoes, deflation caused by degassing may reduce or even cancel any inflation signal caused by magma influx. Nonetheless, detection of pre-eruptive recharge can be achieved by monitoring changes in the long-term deformation rate.

1 Introduction

Persistent passive degassing is observed at volcanoes worldwide (Carn et al., 2017). From 2005–2015, of the 1500 terrestrial volcanoes with possible activity in the Holocene (Siebert et al., 2015), at least 6% (91) were passively degassing above the detection threshold of satellite measurements ($\sim$30 tons day^{-1}) (Carn et al., 2017). Degassing-related hazards depend on gas composition, dispersion, and emission duration. In cases of persistent passive (non-eruptive) degassing, areas of $>$1000 km^2 (e.g., Masaya volcano, Nicaragua) can be affected by acid rain or noxious volcanic smog, as well as fluoride contamination of water (Williams-Jones & Rymer, 2015; Cronin & Sharp, 2002; Allibone et al., 2012).

Cases of sustained high gas flux are mainly observed at volcanoes characterized by open-system degassing. In such systems, exsolved gas within a magma conduit or reservoir segregates from the melt and is released into the atmosphere during non-eruptive periods (Cashman, 2004). Theoretical models show that gas emission can result in a pressure change of a magmatic reservoir, and that pressure changes can also influence gas exsolution (Tait et al., 1989; Boichu et al., 2008, 2011; Anderson & Segall, 2011; Kazahaya et al., 2015). As we show in this study, contrary to the inter-eruptive uplift typ-

ical of the 'classic volcano deformation cycle' (Biggs & Pritchard, 2017), eruptions may be counterintuitively preceded by periods of reservoir depressurization (Girona et al., 2014, 2015).

From 2005–2015, Ambrym (Vanuatu), Kīlauea (Hawai'i), and Nyiragongo (Democratic Republic of Congo) volcanoes were among the ten strongest passively degassing volcanoes on Earth, influenced by the presence of lava lake activity (Carn et al., 2017). At these open-vent volcanoes, surface deformation can be measured by satellite using interferometric synthetic aperture radar (InSAR). While deformation can be used to constrain reservoir overpressure through geodetic modeling, estimates must account for uncertainties on the host rock elastic moduli and reservoir geometry. Combining InSAR deformation measurements with remote sensing gas measurements may provide an opening for long-term studies linking changes in reservoir pressure (and potentially uplift or subsidence) and volcanic degassing. Our study demonstrates this possibility using a multiparametric approach to investigate the effect of volcanic degassing on reservoir pressurization at Ambrym volcano in Vanuatu from 2015–2018. Ambrym is a basaltic volcanic island which hosts a 12-km wide caldera and two main volcanic cones (Marum and Benbow), within which are semi-permanent lava lakes that have been active since at least the 1980's (Robin et al., 1993; Allard et al., 2015). In particular, we investigate a period of inter-eruptive ground subsidence, coinciding with high gas flux, at Ambrym. The subsidence episode preceded a major intrusion crisis that led to the extinction of the lava lakes for more than 2.5 years (at the time of writing, February 2022) (Shreve et al., 2019), after they had been active for at least 3 decades.

To explore physical mechanisms explaining ground subsidence at Ambrym, we first estimate reservoir depressurization rates using geodetic modeling. Then, we use a lumped parameter theoretical model that couples gas emissions with reservoir depressurization, developed in Girona et al. (2014), to explain the estimated depressurization rates and their variation over time. This is the first time the theoretical model of Girona et al. (2014) is applied using observations at an active volcano. The effect of magma replenishment will also be considered to explain an abrupt change in depressurization rate that occurred around October 2017, 14 months before a large dike intrusion and submarine eruption that occurred in December 2018 (Shreve et al., 2019; Hamling et al., 2019; Moussallam et al., 2021). We posit that pre-eruptive reservoir pressurization, associated with magma recharge, may have been balanced by reservoir depressurization due to passive degassing, resulting in a net pressure change of zero prior to the 2018 rift zone eruption, explaining the lack of pre-eruptive uplift.

2 Data and Methods

2.1 2015–2017 Subsidence Episode and 2018 Eruption

InSAR measures ground displacements after a VEI 2 eruption in February 2015, when an intra-caldera vent opened and fed a lava flow (Figure 1a) (Hamling & Kilgour, 2020; Shreve et al., 2021). A time series is processed with the software MintPy (Yunjun et al., 2019) using images acquired by the European Space Agency's satellite constellation Sentinel-1 (S1) (Figure 1a,b and Section 2.3). The first available Sentinel-1 image was acquired on 30 October 2015. The S1 time series and an interferogram from the Japanese

Space Agency's satellite ALOS-2 spanning 21 March 2015 to 28 October 2017 both estimate a maximum subsidence velocity of ∼10 cm year^{-1}. An additional ALOS-2 interferogram indicates the subsidence began between March and June 2015 (Figure S1), after the February 2015 eruption (Section 2.3). The subsidence continued until October 2017, after which it ended abruptly (Figure 1b).

Starting 14 December 2018, 14 months after the end of the subsidence episode, an intra-caldera eruption began at Ambrym, followed by a rift zone intrusion and submarine eruption (Shreve et al., 2019; Hamling et al., 2019; Moussallam et al., 2021). Ambrym's caldera subsided by up to 3 meters, and the lava lakes were completely drained (Shreve et al., 2019; Hamling et al., 2019). Although >0.4 km^3 of magma was intruded into the rift zone (Shreve et al., 2019; Hamling et al., 2019), causing drastic changes to the activity at Ambrym (e.g., lava lake drainage), less than 5 cm of precursory deformation occurred in the year before the event (Figure 1b). Despite a lack of pre-eruptive uplift, two primary observations indicate an increase in magma and gas supply to the system, which may have been precursors to the 2018 eruption. First, a new thermal anomaly ∼1 km to the south of the main lava lake hosted in Marum crater is detected using Sentinel-2 images sometime between 23 June 2016 and 10 March 2018 (Video S1). This indicates either a new vent for gas emissions or the presence of magma close to the surface, although discriminating between the two is ambiguous without additional observations. While the new vent may be a redirection of gas or magma that was already present at depth, its surface manifestation indicates a deviation from background activity. Second, the lava lake level rose rapidly in the weeks before the 2018 eruption, as documented by Moussallam

et al. (2021), which can indicate an increase in magma influx to the system, according to Patrick et al. (2019); Burgi et al. (2020); Global Volcanism Program (2017c).

2.2 2015–2018 SO_2 Gas Emissions

To estimate temporal variation of the sulphur dioxide (SO_2) budget emitted by Ambrym, we calculate the daily SO_2 mass by integrating OMI/Aura SO_2 Total Column over a 150 km-radius circular area centered on Ambrym. We use the Level 2 Version 003 lower tropospheric (TRL) products (corresponding to a center of mass altitude at 3 km (Li et al., 2020)), keeping pixels with a cloud fraction lower than 30% and a column amount greater than 0.3 DU, and removing acquisitions affected by OMI row anomalies. We also remove acquisitions affected by emissions from nearby Ambae volcano in 2017–2018, by discarding dates coinciding with a thermal anomaly at Ambae by MODIS (from MODVOLC (Wright et al., 2004)), and by applying an additional automated procedure relying on the ratio between the gas mass around Ambrym and Ambae (see details in Text S1).

We observe that the daily SO_2 mass burden released passively by Ambrym remains nearly constant between the February 2015 and December 2018 eruptions (Figure 1b). As shown in Figure S2, this observation is consistent with the steadiness of the annual mean SO_2 flux over the 2015–2018 time interval according to the NASA database (`https://so2.gsfc.nasa.gov/kml/OMI_Catalogue_Emissions_2005-2019.xls`, updated following Carn et al. (2017)). The consistency between SO_2 mass and flux also holds from 2005 through to 2019, even if SO_2 flux varied substantially before 2015 (Figure S2). This ex-

cellent consistency indicates that our estimates of SO_2 mass burden at Ambrym, once averaged over several months, are a good proxy of, and nearly proportional to, the SO_2 flux. Since January 2019, SO_2 emissions have reduced to below the detection threshold of satellites, in stark contrast with Ambrym's persistent degassing over the past decade.

We conclude that the SO_2 flux at Ambrym remained essentially constant in the 2015–2018 time interval. Because the major volcanic gas species is H_2O, we assume that the mean SO_2 gas flux in the 2015–2018 time interval (7 kt day^{-1}) can reasonably approximate the mean water vapor gas flux using the mass ratio of $\frac{H_2O}{SO_2} \approx 15$ from the average molar ratios obtained during two field campaign measurements of Ambrym's bulk gas emissions in October 2007 (Table 1 in Allard et al. (2015)). Since there are no estimates of this ratio during the time period of interest, we assume it is constant and discuss the possible effects of a 50% increase or decrease in H_2O flux on our results in Section 4.1.1. We proceed under the assumption that $\hat{Q} = \hat{Q}_{H_2O} \approx 110$ kt day^{-1}.

2.3 Geodetic Inversion

To estimate magma reservoir depressurization, we invert surface displacements measurements spanning March 2015 to October 2017 measured by ALOS-2 and S1. Interferograms were processed using the Interferometric SAR scientific computing environment (ISCE) (Rosen et al., 2012). We multilook ascending S1 interferograms (Track 81) 36 times in range and 12 times in azimuth, filter with a power spectrum filtering strength of 0.3 and unwrap with SNAPHU (Chen & Zebker, 2001). The ascending ALOS-2 interferograms (Track 101) are multilooked 8 times in range and 16 times in azimuth, fil-

tered with a power spectrum filtering strength of 0.2, and unwrapped with a coherence-based NSBAS module ("MPD") described in Shreve et al. (2021). A 12 m TanDEM-X Global DEM is used to remove the topographic phase contribution (Wessel, 2016).

We calculate an S1 InSAR small baseline time series using MintPy with 63 acquisitions to generate and invert 169 interferograms in radar geometry, with temporal baselines ranging from 12 days to 1 year (interferogram network shown in Figure S3) (Yunjun et al., 2019). It is common practice to fit and remove a phase ramp, which may be due to orbital or timing inaccuracies. However, we skip this step because the lack of a non-deforming reference area results in an unstable ramp estimate, which biases the displacement measurements. A comparison of different inversion strategies indicates no meaningful difference between an inversion with uniform weighting and an inversion weighted by the inverse of the phase variance, most likely due to the redundancy of the dense interferometric network (Yunjun et al., 2019) (Figures S3, S4, and Text S3). The two inversion strategies result in different temporal coherence estimates, which determine pixel masking (Figure S4), and we proceed with the time series weighted by the inverse of the phase variance. Finally, we correct the time series for atmospheric effects using the ERA-5 atmospheric model implemented in MintPy with the PyAPS software (Yunjun et al., 2019). The ERA-5 correction is an improvement to the empirical correction based on the relationship between phase delay and elevation (also available in MintPy), which causes spurious jumps in the time series (Figure S5).

Figure 1b shows the displacement time series (acquisitions every 12 days) for various locations at Ambrym from 30 October 2015 to 13 December 2018. Subsidence is mea-

sured, elongated SE-NW within the caldera. The average velocity of the point of maxium subsidence is ∼10 cm year^{-1}, calculated from 30 October 2015 to 31 October 2017, after which subsidence ends. We note that the subsidence stops two months after a seismicity increase on 25 August 2017 (accompanied by a change in eruptive activity), according to a Vanuatu Meteorology and Geo-Hazards Department report (Global Volcanism Program, 2017a) (green vertical line, Figure 1b). Seismicity declined and eruptive activity stabilized by the end of November 2017 (Global Volcanism Program, 2017b). Using the *Defvolc* 3D Mixed Boundary Element Method (BEM) code (Cayol & Cornet, 1997; Fukushima et al., 2005) and Neighborhood Algorithm (Sambridge, 1999b, 1999a) (See Shreve et al. (2021) for a summary of the BEM and Text S2 for a description of the inversion scheme and uncertainty estimation), we perform a joint inversion of the Sentinel-1 velocity map and ALOS-2 ascending interferogram (scaled to obtain displacement in cm year^{-1}). See Text S3 for a detailed description of data preparation for the geodetic modeling, which includes downsampling, estimating the data covariance matrix, and creating the topography mesh.

2.4 Model Coupling Gas Emissions and Reservoir Depressurization

Numerous theoretical models exist to explain pressure change due to degassing processes (i.e., volatile exsolution and escape from a magmatic system) (Tait et al., 1989; Boichu et al., 2008, 2011; Anderson & Segall, 2011). In particular, a theoretical model developed by Girona et al. (2014) addresses the relationship between passive degassing and inter-eruptive reservoir depressurization on timescales of years. Girona et al. (2014) assume the reservoir is connected to the surface by an open conduit, and that the pres-

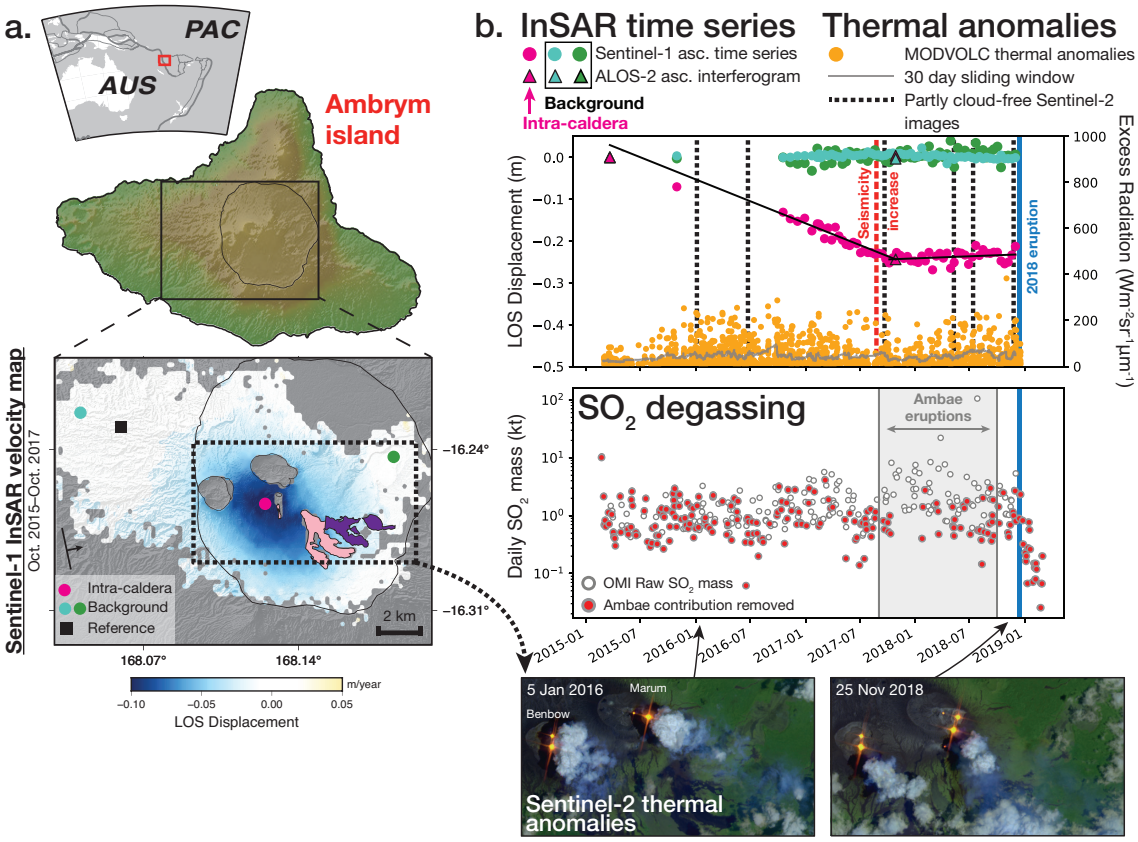

Figure 1: **Time series of InSAR LOS displacement, thermal anomalies, and SO_2 emissions. a.** A tectonic map showing the location of Ambrym island (from Shreve et al. (2019)) and a zoom on Ambrym's caldera, showing the velocity map of the Sentinel-1 ascending time series, assuming deformation spans 30 October 2015–31 October 2017. The caldera is outlined in black, and the extent of the lava flows emplaced in 2015 and 2018 are shown in pink and purple, respectively. The points plotted in the LOS displacement time series are identified with the colored circles (magenta measures displacement inside the deforming caldera, while green and blue measure background displacement near the borders or outside the caldera). The reference point is the black square. **b.** Top figure: The colored dots correspond to the cumulative LOS displacement calculated from a Sentinel-1 ascending time series in three different locations. The triangles outlined in black indicate the cumulative LOS displacement of an ALOS-2 interferogram.

Figure 1: (cont.) The three triangles plotted on 21 March 2015 overlap at 0 m. At each location, the mean of a 3 × 3 pixel box (∼0.6×0.6 km) is calculated. The black dotted lines indicate the (at least partly) cloud-free Sentinel-2 images available during this time period (see Video S1). The orange dots are the excess radiation of thermal anomalies detected within Benbow and Marum craters by the Moderate Resolution Imaging Spectroradiometer (MODIS), which has a pixel size of ∼1×1 km at nadir (Wright et al., 2004; Wright, 2016), and processed using the MODVOLC algorithm. The grey line shows temporal averages calculated using a sliding window of 30 days. Bottom figure: Empty grey dots represent the time-series of raw SO_2 mass burden integrated in an 150 km radius disk around Ambrym from OMI data (TRL product). Red-filled dots represent selected SO_2 mass burden estimates, after removing measurements affected by emissions from the nearby Ambae volcano. The period of elevated volcanic activity at Ambae is indicated by the grey area. Figure adapted from Shreve (2020).

Model	Center (UTM)	Depth (m b.s.l.)	Axis 1 (m)	Ratio Axis 1:Axis 2	Ratio Axis 2:Axis 3	Rotation (°)	V_r (km^3)	ΔV ($\times 10^6$ m^3 year^{-1})	ΔP (MPa year^{-1})
Best-fit	192210 E, 8199170 N	-1880	4700	10	3.6	147	1.2	-3	-2.15
Mean	192367 E ± 1571, 8199425 N ± 1228	-2075 ± 1018	4597 ± 1159	7.9 ± 1.5	5.1 ± 1.9	142 ± 25	N/A	N/A	-3.56 ± 1.63

Table 1: The estimated best-fit ellipsoid model parameters, as well as the mean model and uncertainties (one standard deviation from the mean). Obtained from jointly inverting the Sentinel-1 time series and ALOS-2 interferogram with *Defvolc*. The best-fit ellipsoid is visualized in Figure 2.

Symbol	Description	Range used in this study	Reference
$\frac{\mathrm{d}\Delta P}{\mathrm{d}t}$	pressure change rate during quiescence	-5.2 to -2.0 MPa year^{-1}	This study
$\hat{Q}$	total mean gas flux	110 kt d^{-1}	Carn et al. (2017), Allard et al. (2015)
t	time of passive degassing	∼4 years	This study
R_c	volcanic conduit radius	$\leq$ 300 m	Allard et al. (2016)
V_r	volume of the reservoir	5×10^8 – 3×10^{10} m^3	Shreve et al. (2021)
L	length of the magma column (up to the average reservoir depth)	∼2 km	This study
α	mass fraction of dissolved volatiles in parent melt	1.3 wt%	Allard et al. (2015)
k_r	bulk modulus accounting for chamber compressibility (Text S4)	5×10^8 – 1×10^{10} Pa	Heap et al. (2019)
g	gravity	9.8 m s^{-2}	
$\hat{\rho}_{m,c}$	mean density of melt inside the magma column	2550 kg m^{-3}	Girona et al. (2014)
$\hat{\rho}_{g,c}$	mean density of gas inside the magma column	$\leq$ 200 kg m^{-3}	Girona et al. (2014)
ρ_c	density of fully degassed melt in the column	2670 kg m^{-3}	Girona et al. (2014)
ρ_{nd}	density of the parent undegassed magma	2430 kg m^{-3}	Girona et al. (2014)
γ_c	volume fraction of degassed melt in the magma column	0.5	Girona et al. (2014)

Table 2: A description of the symbols used in Cases 1–3, as well as the ranges chosen for the parameters in this study. Symbols with no range presented are calculated from the defined parameters.

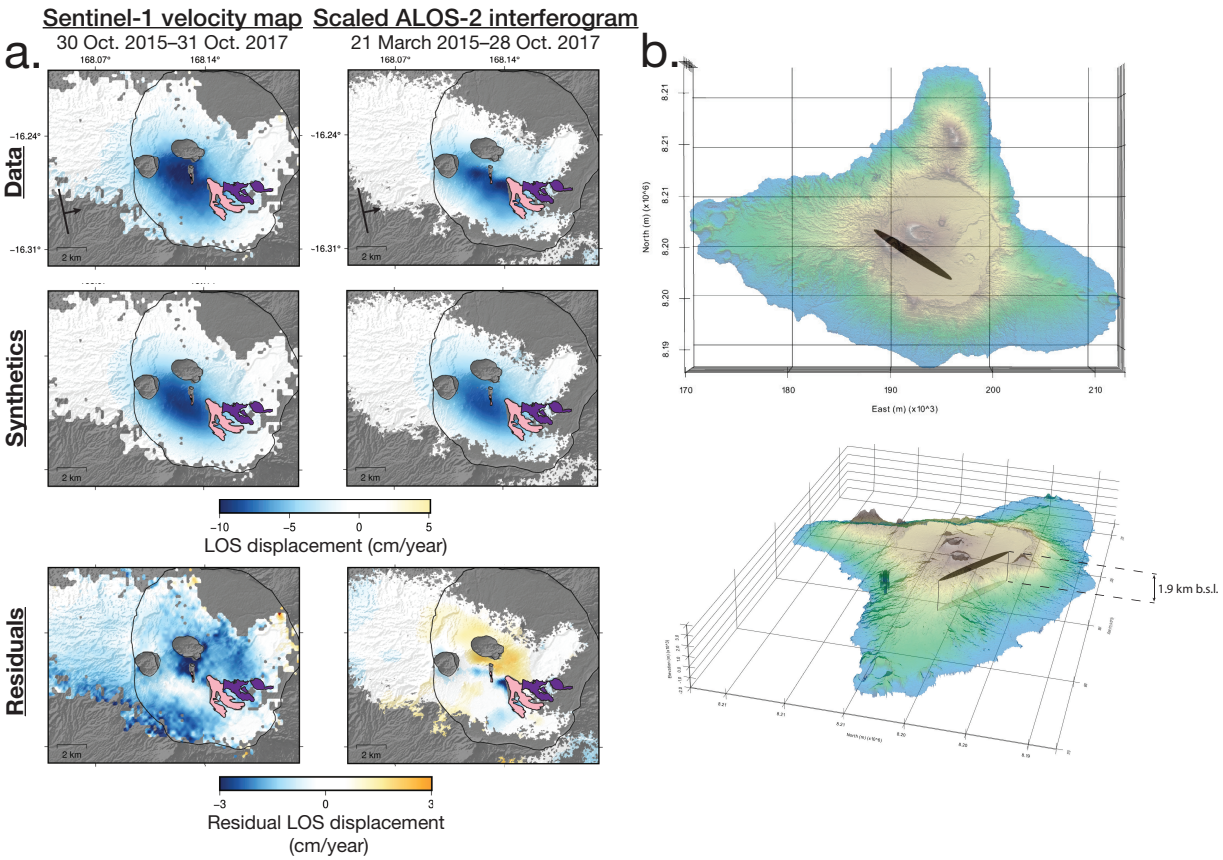

Figure 2: **Inversion results. a.** Geodetic observations (top row), synthetic displacements (middle row) and residuals (bottom row) of an ellipsoid at ∼1.9 km b.s.l (2.8 km beneath the vents). Left column is the Sentinel-1 velocity map, and right column is the ALOS-2 interferogram scaled to obtain displacement in centimeters year^{-1}. The caldera and craters are outlined in black, and the 2015 and 2018 lava flows are shown in pink and purple, respectively. **b.** A map and aerial view of the geometry of the depressurized ellipsoid estimated using *Defvolc*. Plot created with PyVista (Sullivan & Kaszynski, 2019).

sure in the reservoir equilibrates the weight of the magma in the conduit. Consequently, mass changes within the system (either in the conduit or reservoir) due to degassing result in reservoir depressurization, causing ground subsidence. This model takes into account whether volatiles are degassed from the conduit or reservoir, as well as the viscoelastic behavior of the host rock, magma replenishment, and magma density changes. We proceed with this theoretical model to couple passive degassing and reservoir depressurization at Ambrym volcano.

This model simplifies the relationship between mass loss by degassing and reservoir depressurization by assuming the following:

1. A magma reservoir is connected to an open, magma-filled cylindrical conduit with a fixed length L. The reservoir's magma pressure is magmastatic (Figure 3a).
2. Gas mass in the conduit is much smaller than the (incompressible) melt (liquid and solid phase) mass in the conduit (i.e., $m_{m,c}(t) \gg m_{g,c}(t)$).
3. The melt in the conduit is a mixture of an undegassed parent melt and a denser, degassed melt.
4. Gas separation may occur in the conduit or reservoir. Without magma recharge, degassing can continue until the total degassed volatile mass equals that of the initial mass of bulk dissolved volatiles in the undegassed magma.
5. We assume a mean degassing rate $\hat{Q}$ that is constant over months to years. In Section 2.2, we demonstrate that the mean SO_2 flux is constant, while temporal variations in the $\frac{H_2O}{SO_2}$ ratio are unknown and henceforth assumed constant.

6. Crystal content is neglected, temperature (T) of the system is constant, gas solubility depends only on pressure, and the gas mass within the reservoir is calculated at a mean depth.
7. Melt volume decreases during degassing of H_2O. No other volatiles are considered.
8. The host rock of the system is a half-space with a Maxwell viscoelastic rheology (with a bulk modulus k and an effective viscosity μ).

Using these assumptions, this model can be used to gain a first-order understanding of the relationship between a system's degassing flux and depressurization. We investigate whether this model can explain the reservoir depressurization estimated from geodetic models at Ambrym. We then discuss the role of magma replenishment and its effect on the reservoir pressurization rate.

Based on the first assumption above, the pressure change at the base of the conduit at time t can be written as

$$\Delta P(t) = P(t) - P(t_0) = \frac{g(m_{m,c}(t) + m_{g,c}(t))}{\pi R_c(t)^2} - P(t_0), \tag{1}$$

where $P(t)$ and $P(t_0)$ are the pressure within the reservoir at time t and t_0, $m_{m,c}(t)$ is the melt mass within the conduit of constant length L (Figure 3a), $m_{g,c}(t)$ is the gas mass within the conduit, $R_c(t)$ is the conduit radius, and g is gravity. Equation 1 describes a pressurized reservoir which is sustaining the weight of the magma-filled cylindrical conduit, which acts on a surface area of $\pi R_c(t)^2$ (Girona et al., 2014).

Taking the time derivative of this equation, we can obtain the rate of pressure change:

$$\frac{\mathrm{d}\Delta P(t)}{\mathrm{d}t} = \frac{g\hat{\rho}_{m,c}(t)V_{m,c}(t)}{\pi R_c(t)^2}\left\{\frac{1}{\hat{\rho}_{m,c}(t)V_{m,c}(t)}\left[\hat{\rho}_{g,c}(t)\frac{\mathrm{d}V_{g,c}(t)}{\mathrm{d}t} + V_{g,c}(t)\frac{\mathrm{d}\hat{\rho}_{g,c}(t)}{\mathrm{d}t} + \hat{\rho}_{m,c}(t)\frac{\mathrm{d}V_{m,c}(t)}{\mathrm{d}t} + V_{m,c}(t)\frac{\mathrm{d}\hat{\rho}_{m,c}(t)}{\mathrm{d}t}\right] - \frac{2}{R_c(t)}\frac{\mathrm{d}R_c(t)}{\mathrm{d}t}\right\}. \quad (2)$$

We have substituted $m_{m,c}(t) = \hat{\rho}_{m,c}(t)V_{m,c}(t)$ and $m_{g,c}(t) = \hat{\rho}_{g,c}(t)V_{g,c}(t)$, where $\hat{\rho}_{m,c}(t)$, $V_{m,c}(t)$, $\hat{\rho}_{g,c}(t)$, $V_{g,c}(t)$ are the mean melt and gas density and volume in the conduit, respectively.

We further simplify Equation 2 by assuming an elastic host rock, a constant gas and melt density in the conduit ($\frac{\mathrm{d}\hat{\rho}_{g,c}(t)}{\mathrm{d}t} = 0$ and $\frac{\mathrm{d}\hat{\rho}_{m,c}(t)}{\mathrm{d}t} = 0$), a conduit radius that does not change significantly over time ($\frac{\mathrm{d}R_c(t)}{\mathrm{d}t} = 0$), and that the mean gas density in the conduit is significantly smaller than the mean melt density ($\hat{\rho}_{g,c}(t) \ll \hat{\rho}_{m,c}(t)$). We then obtain:

$$\frac{\mathrm{d}\Delta P(t)}{\mathrm{d}t} = \frac{g\hat{\rho}_{m,c}(t)}{\pi R_c(t)^2}\frac{\mathrm{d}V_{m,c}(t)}{\mathrm{d}t}. \quad (3)$$

After considering the relationship between the volume of magma in the reservoir and the partial density of water in a silicate melt, ρ_w, we can rewrite the above equation as:

$$\frac{\mathrm{d}\Delta P(t)}{\mathrm{d}t}\left(\frac{\pi R_c(t)^2}{g\hat{\rho}_{m,c}(t)} + \frac{V_r(t)}{k_r}\right) = -\frac{\hat{Q}}{\rho_w}, \quad (4)$$

which yields, by integration, assuming $\hat{Q}$ is constant, Equation 45 from Girona et al. (2014):

$$\Delta P(t) = -\frac{g\hat{\rho}_{m,c}(t_0)k_r\hat{Q}t}{\pi R_c(t_0)^2\rho_w k + g\rho_w\hat{\rho}_{m,c}(t_0)V_r(t_0)}. \quad (5)$$

The full derivation can be found in Text S4.

Equation 5 can be used to compare the depressurization measured with geodetic modeling (average $\Delta P \propto$ surface deformation) at Ambrym to the theoretical depressurization of the magmatic system by passive degassing (using $\hat{Q}$ as input, using OMI to measure SO_2 mass, then converting to H_2O mass). The remaining parameters necessary to calculate $\Delta P(t)$ are fixed based on previous studies (Table 2—without magma replenishment, Cases 1–3— and Table S1—with magma replenishment, Case 4).

3 Results

3.1 Geodetic Source Estimation

We invert for the location, depth, axes lengths, and pressure change per year of a sub-horizontal ellipsoid beneath Ambrym's caldera (dip fixed to 0°). See Table 1 for the inverted parameters and final geometries. The final estimated source geometry is an ellipsoid elongated N°147 at a depth of ∼2.8 km beneath the craters (1.9 km b.s.l., Figure 2). The northwest tip of the source is located beneath Benbow, and the source extends beneath the caldera for more than 9 km to the SE, oblique to the N°110 rift zone.

The mean pressure change per year of the ellipsoid is -3.56 MPa year^{-1}, ranging between -5.2 to -2.0 MPa year^{-1} when including an error of one standard deviation from the mean (Table 1), given a Young's modulus of 5 GPa and Poisson's ratio of 0.25. The

best-fit model has a pressure change of -2.15 MPa year^{-1} (Table 1). The Young's modulus is estimated from laboratory measurements, according to Heap et al. (2019), yet this parameter is still unconstrained at the scale of the volcanic edifice. These errors are propagated into both the geodetic and theoretical modeling. The Young's modulus may realistically range from 0.5 to 10 GPa. This will affect the estimated pressure change, due to the relationship $\Delta V_r \propto \frac{V_r \Delta P}{G}$ (Anderson & Segall, 2011), where V_r is the volume of the reservoir, ΔV_r and ΔP are its volume and pressure change, respectively, and G is the host rock shear modulus. It follows that the pressure change of the best-fit model may range from -4.2 to -0.2 MPa year^{-1}. A pressure change of -4.2 MPa is within the range of uncertainties from the theoretical model discussed in Section 3.2, while -0.2 MPa could only be obtained with unreasonably large ($V_r > 300$ km^3) reservoir volumes (Section 3.2 and Figure S8). Such uncertainties emphasize the sensitivity of this model to the volcanic conduit and reservoir geometries, which are often unknown. Future studies using seismic wave velocities to calculate the dynamic shear modulus, then converted to the static shear modulus (e.g., Grandin et al., 2010), or using experimental studies of rock samples from the edifice (e.g., Heap et al., 2019), could further constrain the host rock properties.

Because the subsidence rate is approximately constant, we assume that the depressurization rate bounds of -5.2 to -2.0 MPa year^{-1} and the source geometry also remain constant. By combining the depressurization rate with the mean degassing SO_2 flux estimated in Section 2.2, we investigate whether a model coupling mass loss by passive degassing and reservoir depressurization reasonably explains these estimates. We acknowl-

edge that other physical mechanisms may drive subsidence on time scales of months to years, including viscoelastic response of the reservoir tapped during the 2015 eruption (depending on the viscoelastic shell radius and whether the reservoir is refilled) (Segall, 2019), as well as cooling and crystallization of magma (Caricchi et al., 2014; Townsend, 2022). In addition, deformation rates can change abruptly due to energy released from seismic swarms, although typically this occurs during uplift episodes. We conclude that these mechanisms are unlikely because of the relatively short time period of subsidence (2.5 years), the high deformation rate ($\sim$1 cm month^{-1}), and the abrupt end to the subsidence.

3.2 Reservoir Depressurization Rate With No Magma Replenishment

We explore various cases to investigate the effect of the fixed model parameters on reservoir depressurization rate. This includes fixing whether the host-rock is either elastic or viscoelastic, or if gas exsolution occurs in the conduit or reservoir. Finally, we discuss the effect of magma replenishment on the reservoir depressurization rate.

3.2.1 Elastic Rheology (Case 1)

We calculate the theoretical reservoir depressurization rate at Ambrym in an elastic halfspace, for a range of reservoir volumes $V_r(t_0)$ and conduit radii $R_c(t_0)$, given a water vapor flux of $\hat{Q} \approx 110$ kt day^{-1}. The higher the gas flux $\hat{Q}$, the higher the depressurization rate. We also explore a range of reasonable values for the free parameters. For example, the reservoir bulk modulus k_r may realistically vary from 5×10^8 to 1×10^{10} MPa. As k_r increases, the host rock becomes more rigid. On the contrary, if the reser-

voir is compliant, reservoir deformation helps sustain the reservoir's internal pressure. Finally, we fix the initial bulk volatile content, α (used to calculate ρ_w; see Text S4), to 1.3 wt% (Allard et al., 2015). For a given $\hat{Q}$, the lower the value of α, the higher the depressurization rate. This is because for a lower α, a greater volume of magma will need to lose gas to sustain the same $\hat{Q}$. However, for a lower α, the melt density change after degassing would be smaller, which could partly compensate, or even counterbalance, the higher depressurization rate. The density of the parent melt is assumed to be $\rho_{nd} =$ 2430 kg m^{-3} and the density of the degassed melt is $\rho_c = 2670$ kg m^{-3} (values implemented in Girona et al. (2014)). The influence of ρ_{nd} and ρ_c on depressurization rate is shown in Figure S6. Following Girona et al. (2014), we assume steady-state convection in a conduit that consists of 50% parent melt (undegassed) and 50% degassed melt, and the constant mean melt density is $\hat{\rho}_{m,c}(t) = \hat{\rho}_{m,c}(t_0) = 2550$ kg m^{-3}.

Figure 3b shows the theoretical depressurization rates for Case 1 when $k_r = 5 \times 10^8$ Pa, $\hat{Q} = 110$ kt day^{-1}, $\alpha = 1.3$ wt%. According to Shreve et al. (2021), Ambrym's reservoir has a minimum size of 1 km^3. For completeness, we assume a range of reservoir volumes from 1–35 km^3 and conduit radii from 10–700 m. While Allard et al. (2016) inferred a 3 m radius for the upper section of Benbow's conduit to sustain the magma convection needed to explain the SO_2 flux, there have been no direct measurements of the conduit diameter. We therefore investigate a wide range of conduit radii to explore the effect of this parameter on the model outputs. Our models indicate that the depressurization rates at Ambrym inferred from geodesy (between -5.2 and -2 MPa) can be reached for large conduit radii ($R_c > 400$ m) when reservoir volumes are small ($V_r \approx 1$ km^3).

For larger reservoirs ($V_r > 12$ km^3), the conduit radius connecting the lava lakes to the reservoir may be as low as 10 m.

3.2.2 Viscoelastic Rheology, Gas Exsolves in Conduit (Case 2)

Case 1 assumes an elastic half-space, and we wish to investigate how viscoelasticity affects the response of the host rock to mass loss by degassing. We still assume that there is no exsolved gas in the reservoir and introduce a host rock with a Maxwell viscoelastic rheology. Gas is exsolved in and degassed from the conduit of length L, which has an initial gas volume fraction $\beta_c = 0.1$. As in Case 1, we impose steady-state magma convection in the conduit.

Despite the addition of viscoelasticity, for the range of parameters of interest ($V_r =$ 1–35 km^3 and $R_c =$ 10–700 m), no meaningful difference is noted between Case 1 and Case 2 (Figure S7). For larger values of V_r, the solutions begin to diverge when the host rock becomes less viscous ($\mu \approx 10^{17}$ Pa s, Figure S7c). Aside from the minimum viscosity necessary to maintain topography, we have no constraints on this parameter for the host rock at Ambrym. Therefore, we proceed with Case 3 by setting the effective viscosity of the crust to $\mu = 10^{18}$ Pa s (Table S1) and allowing for gas exsolution in the reservoir.

3.2.3 Viscoelastic Rheology, Gas Exsolves in Reservoir (Case 3)

We assume that gases may exsolve within the reservoir according to Henry's Law ($n_r(t) = \alpha - S[P(t_0) - \Delta P(t)]^{\frac{1}{2}}$ when $\alpha > S[P(t_0) + \Delta P(t)]^{\frac{1}{2}}$) (e.g., Huppert & Woods,

2002). Assuming the conduit is completely degassed ($\hat{\rho}_{m,c} = 2670$ kg m^{-3}), and given that $\alpha = 1.3$ wt%, $S = 4{\times}10^{-6}$ Pa$^{-1/2}$ for water, and that $\Delta P(t) \ll P(t_0) = \rho_{m,c} g L \approx$ 52 MPa, the depth of the reservoir when gas exsolution occurs is $L < \frac{1}{g\rho_{m,c}}(\frac{\alpha}{S})^2 \approx 400$ m.

If we assume a slightly larger α (e.g., 2.1 wt% as estimated by Moussallam et al. (2021)), gas exsolution may occur at deeper levels, ∼1 km. This is still too shallow to exsolve bubbles in a reservoir residing at 2–4 km depth, as estimated for the shallowest levels of Ambrym's magmatic system (Shreve et al., 2019, 2021). Geodetic inversions estimate a reservoir depth of ∼2 km beneath Ambrym's lava lakes. We can therefore conclude, according to Henry's Law, that there is no exsolved H_2O in the reservoir. In this case, Case 3 will have the same result as Cases 1 and 2, where gas exsolution occurs within the conduit.

3.3 Reservoir Depressurization Rate With Magma Replenishment (Case 4)

In Section 3.2, depressurization rates estimated at Ambrym from geodetic observations can be obtained using the theoretical model for reservoir volumes > 12 km^3. Using an end member scenario that is consistent with the best-fit mean depressurization rate of -2.15 MPa year^{-1}, we investigate the change in depressurization rate that occurred in October 2017. Between October 2017 (t_0) and December 2018 (t_1), we assume no net depressurization of the magmatic system ($\frac{\mathrm{d}\Delta P(t_1 - t_0)}{\mathrm{d}t} = 0$) because the time series displacements are within the data uncertainty (∼1 cm),.

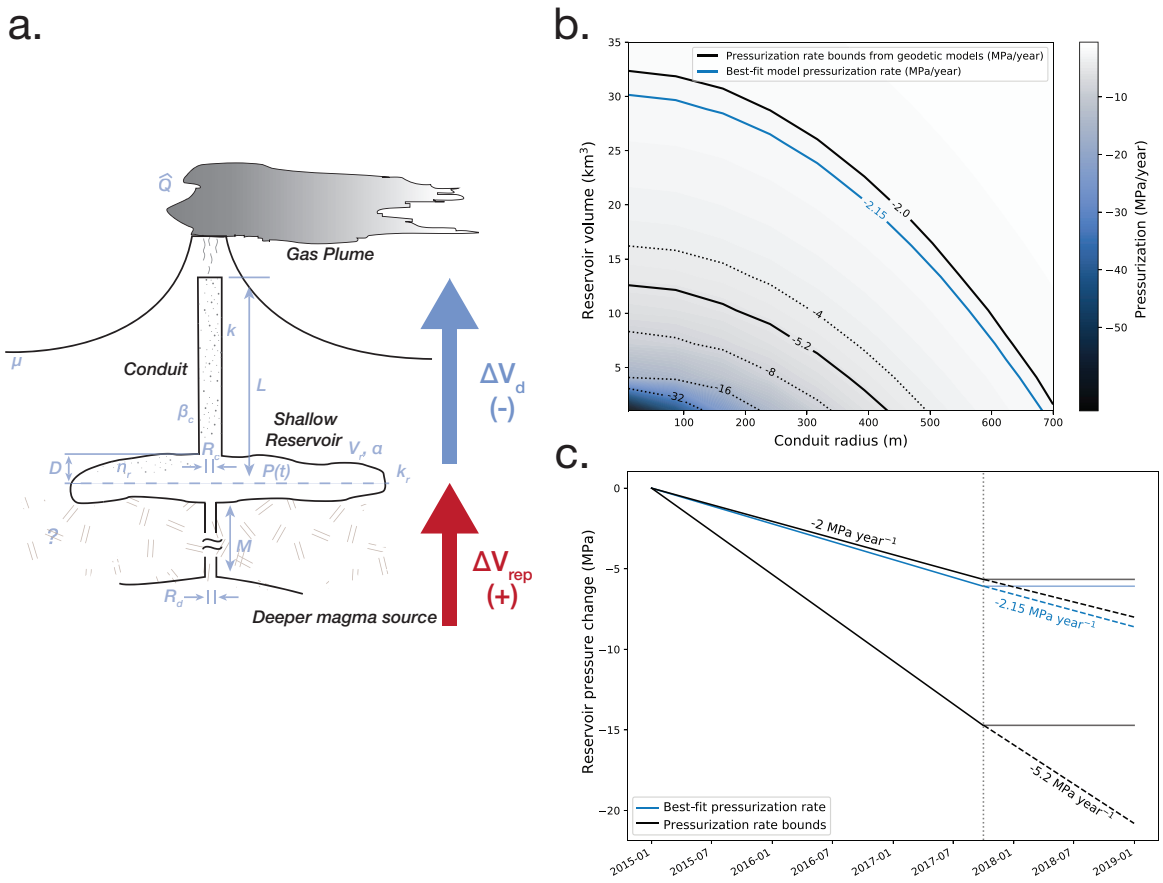

Figure 3: **Degassing-induced depressurization theoretical model. a.** A schematic showing the parameters included in the theoretical model. Modified after Girona et al. (2014). **b.** The pressurization rate change in MPa year^{-1} for a variety of conduit radii and reservoir volumes. The heavy black lines show the upper and lower bounds of the pressure change estimated in the geodetic inversion, and the heavy blue line shows the pressure change of the best-fit model. The dotted contour lines show pressure changes of -32, -16, -8, and -4 MPa year^{-1}. **c.** The reservoir pressure change evolution over time (black and blue corresponding to the upper and lower bounds and best-fit pressure change, respectively), as estimated from geodetic inversions. The vertical dotted line indicates the end of the subsidence episode. The dotted lines show the total reservoir pressure change if no change in the depressurization rate occurred in October 2017.

One possible mechanism that could change the depressurization rate is a decrease in passive degassing. There is, however, no meaningful change in the gas flux measured by satellite during this time period (Figure 1b and Figure S2). Therefore, we hypothesize that the depressurization rate change is due to magma replenishment from a deeper reservoir into the shallow reservoir, counterbalancing the degassing-induced depressurization and resulting in no net pressurization of the shallow reservoir. Building on the previous findings of Cases 1–3, we attempt to constrain the magma replenishment rate. We address two possible scenarios:

1. The deeper source is not overpressurized ($\Delta P_s(t) = 0$). Shallow reservoir depressurization results in a pressure gradient between the shallow and deeper sources. Passive magma replenishment begins as soon as the depressurization began, at the latest in June 2015.
2. Alternatively, the deeper source is overpressurized (i.e., active replenishment, $\Delta P_s(t) > 0$). The deep and shallow sources become (instantaneously) connected in October 2017, and the deep reservoir overpressure remains constant.

Both scenarios will consider a viscoelastic behavior of the host rock. Therefore, we can no longer use the simplified Equation 5 to calculate the reservoir pressure change. Without the simplifications of Equation 2 outlined in Section 2.4, $\frac{\mathrm{d}\Delta P(t)}{\mathrm{d}t}$ is instead expressed as

$$\frac{\mathrm{d}\Delta P(t)}{\mathrm{d}t} = \frac{C_1(t) + C_2(t)\Delta P(t)}{C_3(t)}, \tag{6}$$

where the constants $C_1(t), C_2(t)$, and $C_3(t)$ are functions of the parameters in Equation 2 (See also Equation 34 in Girona et al. (2014), which includes the rate of magma re-

plenishment). The full expansion of these constants and a table of parameters used in this study can be found in Table 2, Text S5, and Table S1.

Following Girona et al. (2014), the pressure change in the shallow reservoir can be expressed with an equation of the form

$$\Delta P(t) = -\Delta P_\infty (1 - e^{-\Gamma t}), \tag{7}$$

where $\Delta P_\infty = \frac{C_1(t_0)}{C_2(t_0)}$ and $\Gamma = -\frac{C_2(t_0)}{C_3(t_0)}$, assuming $C_1(t), C_2(t)$ and $C_3(t)$ do not vary significantly with time from their initial values.

The volumetric rate of magma replenishment is

$$\frac{\mathrm{d}V_{\mathrm{rep}}}{\mathrm{d}t} = \lambda(t)(\Delta P_s(t) - \Delta P(t)), \tag{8}$$

where $\Delta P(t)$ is the pressure change in the shallow reservoir, $\Delta P_s(t)$ is the deep source overpressure, and $\lambda(t)$ is, as defined by Girona et al. (2014), the hydraulic strength (or strength of connectivity between the shallow and deep reservoirs), as derived from the Hagen-Poiseuille law for the volumetric flow rate, given laminar fluid flow in a conduit (Anderson & Segall, 2011; Le Mével et al., 2016).

$$\lambda(t) = \frac{\pi R_d(t)^4}{8 M \mu_{nd}}, \tag{9}$$

where $R_d(t)$ is the radius of the dike connecting the deeper magma source to the shallow reservoir, M is the length of the dike, and μ_{nd} is the viscosity of the replenished, undegassed magma. The maximum Reynold's number $Re = \frac{\rho_m M V_{\mathrm{rep}}}{\pi R_d^2 \mu_m}$, given $\rho_m < 2700$ kg m^{-3}, $V_{\mathrm{rep}} < 5$ m^{3}s^{-1}, $M < 15$ km, $\mu_m > 10^4$ Pa s and $R_d > 2$ m, is ∼1600. This is

smaller than the Re_{crit}∼2000 that defines the bounds between laminar and turbulent flow (Turcotte & Schubert, 2014).

The first scenario addresses passive replenishment, or when the deeper source is not overpressured ($\Delta P_s(t) = 0$). Regardless of the input parameters, the depressurization rate decays exponentially (Equation 7). This decrease is not consistent with the abrupt pressure rate change observed in October 2017 (Figure S9). Therefore, we proceed with the model of active replenishment, considering instead an overpressured deep source ($\Delta P_s(t) > 0$).

As mentioned previously, we assume that a hydraulic connection is created between the deep and shallow reservoirs in October 2017 (t_0), and the connection remains steady until the eruption in December 2018 (t_1). This hydraulic connection may occur when the pressure difference between the shallow and deep reservoirs reaches a critical value, after which any crystallized magma (i.e., a stiff plug) in the connecting dike begins to flow upwards (Girona et al., 2015). As hotter material from the deep reservoir flows into the dike, the dike unplugs and the two reservoirs become hydraulically connected. This unplugging also occurs within two months of the seismicity increase noted by the VMGD (Figure 1b) (Global Volcanism Program, 2017a). As volume is lost during gas emission, the resulting pressure decrease in the shallow reservoir is compensated by a renewed magma inflow from a deeper reservoir, and a pressure balance is obtained in the shallow reservoir ($\Delta P(t_1) - \Delta P(t_0) = 0$). The replenished volume is calculated for each consecutive time step t_{n+1} using Equation 8, given the pressure state of the shallow reservoir at time t_n, a fixed $\lambda(t_0)$, and a $\Delta P_s(t > t_0) > 0$.

As stated in Equation 8, the volume of replenished magma (Figure 4a), is a function of the deep reservoir overpressure $\Delta P_s(t)$, the dike radius and length, and the magma viscosity. Because we have no constraints on these parameters, we instead explore the tradeoff between the lumped parameter $\lambda(t_0)$ (hydraulic strength) and the deep source overpressure $\Delta P_s(t_0)$ (Figure 4c, assuming a $V_r = 29$ km^3 and $R_c = 10$ m, resulting in a shallow reservoir pressure change of ~2.15 MPa year^{-1}). A pressure balance occurs for a wide range of $\Delta P_s(t_0)$ and $\lambda(t_0)$. However, the volume of replenished magma does not vary based on the depressurization rate measured, because the melt volume decrease in the conduit-reservoir system when $\Delta P(t_n) = \Delta P(t_{n+1})$ (i.e., no net pressure change) is also constant and defined by $\frac{\mathrm{d}V_m(t)}{\mathrm{d}t} = \frac{\mathrm{d}V_d(t)}{\mathrm{d}t} + \frac{\mathrm{d}V_{\mathrm{rep}}(t)}{\mathrm{d}t} = \frac{-\hat{Q}}{\rho_w} + \lambda(t_0)(\Delta P_s(t_0) - \Delta P(t))$ (Figure 4a). In the case of no net pressure change, Equation 6 can be simplified to

$$\frac{\mathrm{d}\Delta P(t)}{\mathrm{d}t} = 0 \Longrightarrow \frac{\hat{Q}}{\rho_w} - \lambda(t_0)(\Delta P_s(t_0) - \Delta P(t)) - \frac{\Delta P(t)}{\mu}(V_r(t_0) + V_{m,c}(t_0)) = 0, \quad (10)$$

where volume change is determined by the balance between volume loss due to degassing, volume increase due to magma influx, and the viscous response of the conduit and reservoir. As shown in Figure 4a, the total replenished volume necessary to create a pressure balance $\Delta P(t_{n+1}) - \Delta P(t_n) = 0$ within the shallow reservoir is ~0.16 km^3 over 14 months, or a magma supply rate into the shallow reservoir of ~4.3 m^3 s^{-1}.

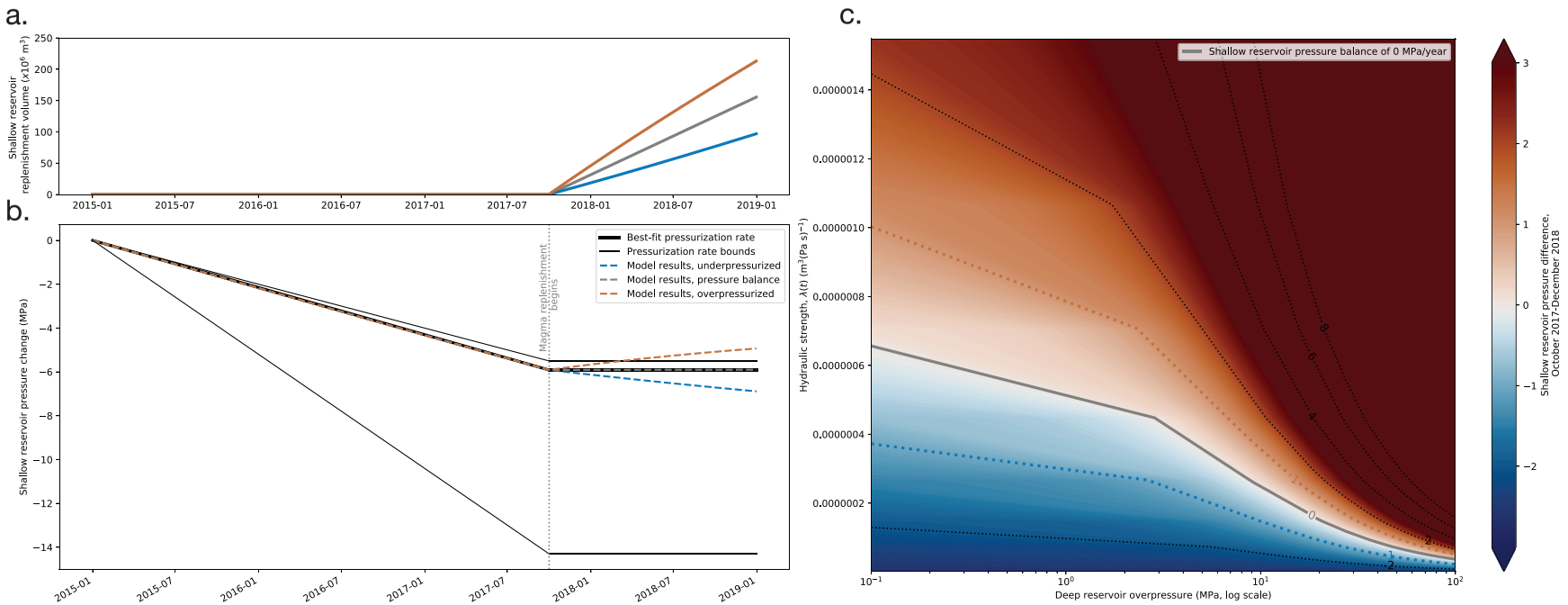

Figure 4: **Effect of magma replenishment. a.** The replenishment volume over time for three cases: an overpressurized and underpressurized reservoir (pink and blue lines, respectively) at t_1 (December 2018) and a reservoir with a pressure balance (grey line). **b.** The lower and upper bounds and best-fit shallow reservoir pressurization bounds (thin and thick black lines, respectively) over time as estimated from the theoretical model (Figure 3b for reasonable V_r and R_c that correspond to these values). The vertical dotted line represents when the deeper reservoir becomes instantaneously overpressurized. **c.** The relationship between shallow reservoir pressure difference between t_0 (October 2017) and t_1 (December 2018), hydraulic strength, and deep reservoir overpressure $\Delta P_s(t_0)$. The parameters that lead to a pressure balance in the shallow reservoir ($\Delta P = 0$) are indicated by the black line, and an overpressurized ($\Delta P > 0$) and underpressurized ($\Delta P < 0$) shallow reservoir by the pink and blue dotted lines, respectively.

4 Discussion

4.1 Volume of Ambrym's Reservoir

Using a simplified conceptual model of a volcanic plumbing system (a single conduit hydraulically connected to a shallow reservoir fed by a deep source), the subsidence rates at Ambrym estimated with geodetic models can be obtained with a smaller reservoir volume ($V_r \approx 1$ km^3) and a conduit radius of >400 m. We consider this unrealistic based on studies showing that conduit radii are <200 m (e.g., Stephens et al., 2017). As mentioned previously, the upper section of Benbow's conduit is estimated to have a radius of 3 m (Allard et al., 2016). This narrow conduit would be consistent, given our calculations, with a magma reservoir volume >12 km^3.

Previous estimates of Ambrym's shallow magmatic reservoir have ranged from 0.5 (Allard et al., 2015) to 9.5 km^3 (Shreve et al., 2021), with no estimates in the range of >12 km^3. This may imply one of the following:

1. The model is oversimplified, and does not represent Ambrym's plumbing system,

   or

2. previous reservoir volume estimates are underestimated.

We address each of these possibilities in turn.

4.1.1 Model Parameters Affecting Depressurization Rates

Given the high gas flux at Ambrym, the geodesy-derived depressurization rates require a large reservoir because it will need to be subjected to a smaller pressure change

to result in the same volume change due to gas emissions (recall $\Delta V_r \propto \frac{V_r \Delta P}{G}$). In this study, the geometry of the reservoir-conduit system is simplified. We assume a single conduit extending from the surface to 2 km b.s.l., from which gas can exsolve and escape, causing magma convection in the conduit. Volcanic conduits have been imaged to depths of up to a few hundred meters within the edifice using muon tomography (Tanaka et al., 2009), but at deeper depths (>1 km) magma ascent is thought to occur by porous flow through the thermally weakened, yet crystal-rich host rock (McKenzie, 1984). In addition, Ambrym has two active craters with multiple vents that were passively degassing during the time period of interest, and their connection at depth is not understood. Throughout this study, we assume a single conduit connects the reservoir to the surface, which may oversimplify reality.

Another factor that affects the pressure change within the reservoir, but is not considered in this model, is magma compressibility. Withdrawal of a compressible magma from the system mutes reservoir pressure changes, because magma volume increases as the magma ascends and decompresses. Therefore, the magma density in the reservoir should be considered to account for this volume change, similar to Case 3 (when gas exsolves in the reservoir). However, using the pressure-dependent model based on Henry's law, no water vapor exsolves at depths of ∼2 km. Past studies of Ambrym indicate that magma compressibility in the reservoir may be higher than for gas-poor basalts (Shreve et al., 2021; Hamling & Kilgour, 2020). These results imply that magma compressibility at Ambrym may be high enough to cause larger reservoir volume estimates, but the full implications of magma compressibility are outside this study's scope.

In addition, due to the unconstrained depth of the deeper reservoir, we assume that InSAR surface displacements are only influenced by pressurization of the shallow reservoir (Du et al., 1992; Rivalta & Segall, 2008). Petrological constraints from previous work (e.g., Moussallam et al. (2021)) based on melt inclusion entrapment pressures from the 2018 eruptive products indicate that magma may be stored at depths of up to 9.5 km b.s.l. Clinopyroxene barometry estimates a magma plumbing system that reaches depths of 14 km b.s.l. (Firth et al., 2016; Sheehan & Barclay, 2016). However, given that only one melt inclusion from the 2018 eruption was used to estimate the depth of 9.5 km b.s.l. (Moussallam et al., 2021), we cannot robustly constrain the deeper reservoir location. Assuming a spherical point pressure source (Mogi, 1958), an elastic medium, and the estimated magma influx ($\sim$0.16 km^3), the reservoir would need a depth >25 km for subsidence to be <5 cm in the satellite LOS. This reservoir may be shallower than 25 km if magma compressibility results in muted ground displacements, however, as mentioned previously, we do not further explore effects of magma compressibility.

Finally, as mentioned in Section 2.2, the H_2O flux used to estimate the depressurization rate is based on the assumption of a constant $\frac{H_2O}{SO_2}$ ratio, as well as a SO_2 CMA at 3 km. If these assumptions are incorrect, the H_2O flux used as input for the theoretical model would be biased. Therefore, we run the model for H_2O fluxes $\pm$50% (55 or 165 kt; Figure S10). The estimated reservoir volume is >5 km^3 for a conduit radius $R_c \sim$ 10 m, and the total replenished volume is $V_{rep} = 0.077$ km^3 when $\hat{Q} = 55$ kt and 0.232 km^3 when $\hat{Q} = 165$ kt.

505 #### *4.1.2 Underestimation of Reservoir Volume Estimates*

506 Previous studies have put bounds on Ambrym's reservoir volume using either magma
507 chamber residence times (Allard et al., 2015), or with geodesy (Shreve et al., 2021). The
508 former estimated a minimum reservoir volume of 0.5 km^3 at depths of ∼3.8 km below
509 the summit according to the magma influx rate needed to explain the mean SO_2 plume
510 flux (∼7800 tons day^{-1}) (Allard et al., 2015; Bani et al., 2012). Allard et al. (2015) ac-
511 knowledge that this reservoir is connected to the lava lakes by a shallower plumbing sys-
512 tem, which we hypothesize is the depressurized reservoir imaged with geodesy in this study.
513 In addition, they conclude that in order to accommodate the recycling of degassed magma,
514 the magma plumbing system must be larger than 0.5 km^3.

515 By relating geodetic models to the SO_2 flux measured by OMI satellite-based UV
516 spectrometers, Shreve et al. (2021) estimates that the minimum reservoir size is 1 km^3,
517 with possible reservoir volumes as high as 9.5 km^3. However, these may also be under-
518 estimates, because they depend on the assumed host rock shear modulus, which is not
519 well constrained at Ambrym. This study cannot further constrain the upper bound on
520 the size of the degassed reservoir at Ambrym. Nonetheless, the results presented here
521 are consistent with the conclusions that previous studies have underestimated the reser-
522 voir volume, and that it may be as large as 12 km^3.

4.2 Magma Replenishment Prior to the 2018 Eruption

4.2.1 Magma Supply Rate

According to our study, approximately 0.16 km^3 of magma would have been needed to replenish the shallow reservoir to counteract the subsidence from degassing, equivalent to a magma supply rate into the shallow reservoir $\frac{dV_{rep}}{dt} \approx 4.3$ m^3 s^{-1}. In a previous study, Allard et al. (2015) estimates that 25 m^3 s^{-1} of magma is necessary to sustain the SO_2 flux released at the surface. However, the estimate from Allard et al. (2015) corresponds to the volume of the magma batch that loses its gas and is recycled deeper in the system per unit time. On the other hand, our estimate corresponds to the volume lost in this recycling process, due to density changes during degassing, hence representing a fraction of the recycled volume of Allard et al. (2015). The ratio between the two estimates is approximately equal to a "shrinkage ratio" $\beta = \frac{\rho_c - \rho_{nd}}{\rho_{nd}} = \frac{\Delta\rho}{\rho_{nd}} \approx 10\%$, defined as the density increase of the magma due to degassing (see Text S6 for a detailed derivation).

The magma supply rate estimated in this study (4.3 m^3 s^{-1}) is on the same order of magnitude as the mantle-driven surge in magma supply rate at Kīlauea in 2006, during the eruption from the Pu'u 'Ō'ō–Kupaianaha vent system which began in 1983 (Poland et al., 2012). The supply rate was estimated to range between 6–7 m^3 s^{-1}, depending on the assumed magma compressibility (Poland et al., 2012). This estimate was made using a calculation similar to Allard et al. (2015), with SO_2 flux used as a proxy for lava effusion rates and consequently magma supply rate (Poland et al. (2012) also includes volume change due to geodetic modeling of uplift that occurred in 2006). However, at

Kīlauea, the degassed magma is assumed to have erupted from the Pu'u Ō'ō vent (as opposed to being recycled) and been replenished at the same rate with magma from depth. Therefore, these calculations are more comparable to our estimate than the supply rate estimated by Allard et al. (2015).

4.2.2 Stealth Magma Replenishment

Recent conceptual models describe volcanic unrest and eruption (in particular initial conduit formation) in three phases. The first is "staging", which can occur either at the end of a previous eruption, during intereruptive time periods, or immediately preceding an eruption (Roman & Cashman, 2018). In the case of replenishment at Ambrym, the latter seems the most likely. Earthquakes detected in mid-2017 were the first indication of magma replenishment to shallower levels (Global Volcanism Program, 2017a), possibly indicating the shear failure of host rocks due to a magma intrusion. Further analysis of seismic data is necessary to discriminate between the processes causing seismicity in August 2017.

Around the same time, the number of active vents increased, also indicating a magma influx into the system (Video S1). After an increase in lava lake level (Moussallam et al., 2021), the shallow reservoir destabilized, causing the initial intra-caldera eruption of 14 December 2018, and eventually tapped the deeper magmatic system the following day (Shreve et al., 2019). The deeper portion of the magmatic system (>6.5 km b.s.l.) fed the rift zone intrusion and submarine eruption, according to melt inclusion entrapment pressures (Moussallam et al., 2021).

The pressure balance due to the combined effects of degassing and magma replenishment results in a low stress change on the host rocks, effectively equivalent to a "rate or volume that is too low/small to produce detectable seismicity" (Roman & Cashman, 2018). This demonstrates the possibility of a replenishment volume and rate that is large compared to other geodetically-derived magma replenishment rates (e.g., 187 $\times 10^6$ m^3 over 7.3 years at Laguna del Maule (Le Mével et al., 2016)) without notable seismicity in the months prior to the eruption (according to VMGD reports).

5 Conclusion

This study attempts to quantify the influence of persistent degassing on the pressurization state of a magma reservoir, ultimately allowing for more accurate forecasts of future activity. The theoretical model is a simplistic view of reality (e.g., only one shallow reservoir and conduit, assumes steady conduit convection, etc.), but the uncertainties and tradeoffs presented in this study may be further reduced at a volcanic system with more instrumentation, or a longer time series of passive degassing and ground displacement.

Despite the theoretical model's simplifications, we can conclude that:

1. continuous passive degassing is a plausible mechanism to drive ~2.5 years of reservoir depressurization and subsidence at Ambrym volcano, and
2. "stealth" replenishment of magma may have occurred in the 14 months prior to the 2018 eruption, resulting in a net pressure balance in the shallow magmatic sys-

tem, explaining the abrupt cessation of subsidence in October 2017 and the absence of pre-eruptive uplift prior to the December 2018 eruption.

These findings have implications for the monitoring of Ambrym volcano. InSAR geodesy demonstrates a lack of substational uplift (<5 cm, Figure 1b) in the 12 days prior to the 2018 eruption. However, InSAR detected changes in the long-term deformation trend, in particular the abrupt end of a subsidence episode after 2.5 years. We interpret the subsequent lack of subsidence as indirect evidence for magma influx from depth in the 14 months preceding the 2018 eruption, a conclusion that cannot be drawn from degassing and thermal anomalies alone. As quantitative in-situ measurements (such as GNSS or gravity measurements and lava lake level heights) are seldom available, multiparametric remote sensing observations (radar, gas and thermal satellite imagery) provide an alternative means of detecting magma replenishment over time scales of months to years before eruptions.

Acknowledgments

We thank the Japan Aerospace Exploration Agency (JAXA 6th Research agreement no. 3245) and the European Space Agency (ESA) for providing access to the radar imagery used in this study. A portion of the ALOS-2 data was provided under a cooperative research contract between Geospatial Information Authority of Japan and JAXA. The ownership of ALOS-2 data belongs to JAXA. We would like to thank Francisco Delgado, Hélène Le Mével, Yan Zhan, Társilo Girona, and Patrick Allard for thoughtful discussions and insights which helped bring this manuscript to fruition. The authors would

607 also like to thank two anonymous reviewers and the editor for their constructive com-
608 ments. Several calculations used the S-CAPAD cluster of IPGP. Marie Boichu would like
609 to acknowledge support from the VOLCPLUME ANR project (ANR-15-CE04-0003-01).
610 This project has also received funding from the European Union's Horizon 2020 research
611 and innovation program under the Marie Skłodowska-Curie grant agreement no. 665850.
612 We also acknowledge support from the FAIR-EASE project, which received funding from
613 the European Union's Horizon Europe Framework Programme (HORIZON) under grant
614 agreement No. 101058785. This is IPGP contribution number 4263.

615 References

616 Allard, P., Aiuppa, A., Bani, P., Métrich, N., Bertagnini, A., Gauthier, P., ...
617 Garaebiti, E. (2015). Prodigious emission rates and magma degassing bud-
618 get of major, trace and radioactive volatile species from Ambrym basaltic
619 volcano, Vanuatu Island arc. *Journal of Volcanology and Geothermal Research*,
620 *304*, 378 – 402. doi: https://doi.org/10.1016/j.jvolgeores.2015.10.004
621 Allard, P., Burton, M., Sawyer, G., & Bani, P. (2016). Degassing dynamics
622 of basaltic lava lake at a top-ranking volatile emitter: Ambrym volcano,
623 Vanuatu arc. *Earth and Planetary Science Letters*, *448*, 69–80. Re-
624 trieved from `http://dx.doi.org/10.1016/j.epsl.2016.05.014` doi:
625 10.1016/j.epsl.2016.05.014
626 Allibone, R., Cronin, S., Charley, D., Neall, V., Stewart, R., & Oppenheimer, C.
627 (2012). Dental fluorosis linked to degassing of Ambrym volcano, Vanuatu:
628 A novel exposure pathway. *Environmental Geochemistry and Health*, *34*(2),

155–170. doi: 10.1007/s10653-010-9338-2

Anderson, K., & Segall, P. (2011). Physics-based models of ground deformation and extrusion rate at effusively erupting volcanoes. *Journal of Geophysical Research: Solid Earth*, *116*(7), 1–20. doi: https://doi.org/10.1029/2010JB007939

Bani, P., Oppenheimer, C., Allard, P., Shinohara, H., Tsanev, V., Carn, S., ... Garaebiti, E. (2012). First estimate of volcanic SO_2 budget for Vanuatu Island arc. *Journal of Volcanology and Geothermal Research*, *211-212*, 36–46.

Biggs, J., & Pritchard, M. (2017). Global volcano monitoring: What does it mean when volcanoes deform? *Elements*, *13*(1), 17–22. doi: 10.2113/gselements.13.1.17

Boichu, M., Villemant, B., & Boudon, G. (2008). A model for episodic degassing of an andesitic magma intrusion. *Journal of Geophysical Research: Solid Earth*, *113*(7), 1–18. doi: https://doi.org/10.1029/2007JB005130

Boichu, M., Villemant, B., & Boudon, G. (2011). Degassing at La Soufrière de Guadeloupe volcano (Lesser Antilles) since the last eruptive crisis in 1975-77: Result of a shallow magma intrusion? *Journal of Volcanology and Geothermal Research*, *203*(3-4), 102–112. doi: https://doi.org/10.1016/j.jvolgeores.2011.04.007

Burgi, P., Boudoire, G., Rufino, F., Karume, K., & Tedesco, D. (2020). Recent Activity of Nyiragongo (Democratic Republic of Congo): New Insights From Field Observations and Numerical Modeling. *Geophysical Research Letters*,

651 *47*(17). doi: 10.1029/2020GL088484

652 Caricchi, L., Biggs, J., Annen, C., & Ebmeier, S. (2014). The influence of cool-
653 ing, crystallisation and re-melting on the interpretation of geodetic signals
654 in volcanic systems. *Earth and Planetary Science Letters*, *388*, 166–174.
655 Retrieved from `http://dx.doi.org/10.1016/j.epsl.2013.12.002` doi:
656 10.1016/j.epsl.2013.12.002

657 Carn, S., Fioletov, V., Mclinden, C., Li, C., & Krotkov, N. (2017). A decade of
658 global volcanic SO_2 emissions measured from space. *Scientific Reports*, *7*, 1–
659 12. doi: http://doi.org/10.1038/srep44095

660 Cashman, K. (2004). Volatile controls on magma ascent and eruption. *Geophysical*
661 *Monograph Series*, *150*, 109–124. doi: http://doi.org/10.1029/150GM10

662 Cayol, V., & Cornet, F. (1997). 3D mixed boundary elements for elastostatic defor-
663 mation field analysis. *International journal of rock mechanics and mining ...*,
664 *34*(2), 275–287. doi: http://doi.org/10.1016/S0148-9062(96)00035-6

665 Chen, C., & Zebker, H. (2001). Two-dimensional phase unwrapping with use of sta-
666 tistical models for cost functions in nonlinear optimization. *Journal of the Op-*
667 *tical Society of America A*, *18*(2), 338. doi: 10.1364/JOSAA.18.000338

668 Cronin, S., & Sharp, D. (2002). Environmental impacts on health from contin-
669 uous volcanic activity at Yasur (Tanna) and Ambrym, Vanuatu. *Inter-*
670 *national Journal of Environmental Health Research*, *12*(2), 109–123. doi:
671 10.1080/09603120220129274

672 Du, Y., Aydin, A., & Segall, P. (1992). Comparison of various inversion techniques

as applied to the determination of a geophysical deformation model for the 1983 Borah Peak earthquake. *Society*, *82*(4), 1840–1866.

Firth, C., Handley, H., Turner, S., Cronin, S., & Smith, I. (2016). Variable conditions of magma storage and differentiation with links to eruption style at Ambrym volcano, Vanuatu. *Journal of Petrology*, *57*(6), 1049–1072. doi: 10.1093/petrology/egw029

Fukushima, Y., Cayol, V., & Durand, P. (2005). Finding realistic dike models from Interferometric Synthetic Aperture Radar data: The February 2000 eruption at Piton de la Fournaise. *Journal of Geophysical Research: Solid Earth*, *110*(3), 1–15. doi: http://doi.org/10.1029/2004JB003268

Girona, T., Costa, F., Newhall, C., & Taisne, B. (2014). On depressurization of volcanic magma reservoirs by passive degassing. *Journal of Geophysical Research : Solid Earth*, *119*, 8667–8687. doi: https://doi.org/10.1002/2014JB011368

Girona, T., Costa, F., & Schubert, G. (2015). Degassing during quiescence as a trigger of magma ascent and volcanic eruptions. *Scientific Reports*, *5*, 1–7. doi: 10.1038/srep18212

Global Volcanism Program. (2017a). Report on Ambrym (Vanuatu). *Weekly Volcanic Activity Report, 30 August-5 September 2017*. Retrieved from `https://volcano.si.edu/showreport.cfm?doi=GVP.WVAR20170830-257040`

Global Volcanism Program. (2017b). Report on Ambrym (Vanuatu). *Weekly Volcanic Activity Report, 6 December-12 December 2017*. Retrieved from `https://volcano.si.edu/showreport.cfm?doi=GVP.WVAR20171206-257040`

Global Volcanism Program. (2017c). Report on Erta 'Ale (Ethiopia). *Weekly Volcanic Activity Report, 25 January–31 January 2017*. Retrieved from `https://volcano.si.edu/showreport.cfm?doi=GVP.WVAR20170125-221080`

Grandin, R., Socquet, A., Jacques, E., Mazzoni, N., De Chabalier, J., & King, G. (2010). Sequence of rifting in Afar, Manda-Hararo rift, Ethiopia, 2005-2009: Time-space evolution and interactions between dikes from Interferometric Synthetic Aperture Radar and static stress change modeling. *Journal of Geophysical Research: Solid Earth*, *115*(10), 2005–2009. doi: http://doi.org/10.1029/2009JB000815

Hamling, I., Cevuard, S., & Garaebiti, E. (2019). Large-Scale Drainage of a Complex Magmatic System: Observations From the 2018 Eruption of Ambrym Volcano, Vanuatu. *Geophysical Research Letters*, *46*(9), 4609–4617. doi: 10.1029/2019GL082606

Hamling, I., & Kilgour, G. (2020). Goldilocks conditions required for earthquakes to trigger basaltic eruptions : Evidence from the 2015 Ambrym eruption. *Science Advances*, *6*(14).

Heap, M., Villeneuve, M., Albino, F., Farquharson, J., Brothelande, E., Amelung, F., ... Baud, P. (2019). Towards more realistic values of elastic moduli for volcano modelling. *Journal of Volcanology and Geothermal Research*, 106684. doi: http://doi.org/10.1016/j.jvolgeores.2019.106684

Huppert, H., & Woods, A. (2002). The role of volatiles in magma chamber dynamics. *Nature*, *420*(6915), 493–495. doi: 10.1038/nature01211

717 Kazahaya, R., Aoki, Y., & Shinohara, H. (2015). Budget of shallow magma plumb-
718 ing system at Asama Volcano, Japan, revealed by ground deformation and
719 volcanic gas studies. *Journal of Geophysical Research: Solid Earth*, *120*, 2961–
720 2973. doi: 10.1002/2015JB012608.Received

721 Le Mével, H., Gregg, P., & Feigl, K. (2016). Magma injection into a long-lived
722 reservoir to explain geodetically measured uplift: Application to the 2007–2014
723 unrest episode at Laguna del Maule volcanic field, Chile. *Journal of Geophysi-*
724 *cal Research: Solid Earth*, *121*(8), 6092–6108. doi: 10.1002/2016JB013066

725 Li, C., Krotkov, N., Leonard, P., & Joiner, J. (2020). *OMI/Aura Sulphur Dioxide*
726 *(SO_2) Total Column 1-orbit L2 Swath 13×24 km V003.* Accessed: 8 February
727 2022. doi: 10.5067/Aura/OMI/DATA2022

728 McKenzie, D. (1984). The generation and compaction of partial melts. *J. Petrol.*,
729 *25*, 713–765.

730 Mogi, K. (1958). Relations between the eruptions of various volcanoes and the de-
731 formations of the ground surfaces around them. *Bulletin of the Earthuake Re-*
732 *search Institute*, *36*, 99–134.

733 Moussallam, Y., Médard, E., Georgeais, G., Rose-koga, E., Koga, K., Pelletier, B.,
734 ... Peters, N. (2021). How to turn off a lava lake ? A petrological investiga-
735 tion of the 2018 intra-caldera and submarine eruptions of Ambrym volcano.
736 *Bulletin of Volcanology*, *83*(36), 1–19.

737 Patrick, M., Swanson, D., & Orr, T. (2019). A review of controls on lava lake level:
738 insights from Halema‘uma‘u Crater, Kīlauea Volcano. *Bulletin of Volcanology*,

81(3). doi: 10.1007/s00445-019-1268-y

Poland, M., Miklius, A., Jeff Sutton, A., & Thornber, C. (2012). A mantle-driven surge in magma supply to Kīlauea Volcano during 2003-2007. *Nature Geoscience*, *5*(4), 295–300. Retrieved from `http://dx.doi.org/10.1038/ngeo1426` doi: 10.1038/ngeo1426

Rivalta, E., & Segall, P. (2008). Magma compressibility and the missing source for some dike intrusions. *Geophysical Research Letters*, *35*(4), 0–4. doi: http://doi.org/10.1029/2007GL032521

Robin, C., Eissen, J., & Monzier, M. (1993). Giant tuff cone and 12-km-wide associated caldera at Ambrym Volcano (Vanuatu, New Hebrides Arc). *Journal of Volcanology and Geothermal Research*, *55*(3-4), 225–238. doi: 10.1016/0377-0273(93)90039-T

Roman, D., & Cashman, K. (2018). Top–Down Precursory Volcanic Seismicity: Implications for 'Stealth' Magma Ascent and Long-Term Eruption Forecasting. *Frontiers in Earth Science*, *6*(September), 1–18. doi: 10.3389/feart.2018.00124

Rosen, P., Gurrola, E., Sacco, G., & Zebker, H. (2012, April). The InSAR scientific computing environment. In *Eusar 2012; 9th european conference on synthetic aperture radar* (p. 730-733).

Sambridge, M. (1999a). Geophysical inversion with a neighbourhood algorithm – II. Appraising the ensemble. *Geophysical Journal International*, *138*(2), 727–746. doi: http://doi.org/10.1046/j.1365-246X.1999.00876.x

761 Sambridge, M. (1999b). Geophysical inversion with a neighbourhood algorithm – I.
762 Searching a parameter space. *Geophysical Journal International*, *138*, 479–494.
763 doi: http://doi.org/10.1046/j.1365-246x.1999.00900.x

764 Segall, P. (2019). Magma chambers: What we can, and cannot, learn from volcano
765 geodesy. *Philosophical Transactions of the Royal Society A: Mathematical,*
766 *Physical and Engineering Sciences*, *377*(2139). doi: http://doi.org/10.1098/
767 rsta.2018.0158

768 Sheehan, F., & Barclay, J. (2016). Staged storage and magma convection at Am-
769 brym volcano, Vanuatu. *Journal of Volcanology and Geothermal Research*,
770 *322*, 144–157. doi: http://doi.org/10.1016/j.jvolgeores.2016.02.024

771 Shreve, T. (2020). *Crustal deformation at Ambrym (Vanuatu) imaged with satel-*
772 *lite geodesy: constraints on magma storage, migration, and outgassing* (Doc-
773 toral dissertation, Institut de Physique du Globe de Paris). Retrieved from
774 `https://tel.archives-ouvertes.fr/tel-03171509`

775 Shreve, T., Grandin, R., Boichu, M., Garaebiti, E., Moussallam, Y., Ballu, V., ...
776 Pelletier, B. (2019). From prodigious volcanic degassing to caldera subsidence
777 and quiescence at Ambrym (Vanuatu): the influence of regional tectonics. *Sci-*
778 *entific Reports*, *9*(18868). doi: https://doi.org/10.1038/s41598-019-55141-7

779 Shreve, T., Grandin, R., Smittarello, D., Cayol, V., Pinel, V., Boichu, M., & Mor-
780 ishita, Y. (2021). What triggers caldera ring-fault subsidence at Ambrym
781 volcano? Insights from the 2015 dike intrusion and eruption. *Journal of Geo-*
782 *physical Research: Solid Earth*, *126*.

Siebert, L., Cottrell, E., Venzke, E., & Andrews, B. (2015). *Earth's Volcanoes and Their Eruptions: An Overview* (Second Edition ed.) (No. 1). Elsevier. Retrieved from http://dx.doi.org/10.1016/B978-0-12-385938-9.00012-2 doi: 10.1016/b978-0-12-385938-9.00012-2

Stephens, K., Ebmeier, S., Young, N., & Biggs, J. (2017). Transient deformation associated with explosive eruption measured at Masaya volcano (Nicaragua) using Interferometric Synthetic Aperture Radar. *Journal of Volcanology and Geothermal Research*, *344*, 212–223.

Sullivan, C. B., & Kaszynski, A. (2019, May). PyVista: 3D plotting and mesh analysis through a streamlined interface for the Visualization Toolkit (VTK). *Journal of Open Source Software*, *4*(37), 1450. Retrieved from https://doi.org/10.21105/joss.01450 doi: 10.21105/joss.01450

Tait, S., Jaupart, C., & Vergniolle, S. (1989). Pressure, gas content and eruption periodicity of a shallow, crystallising magma chamber. *Earth and Planetary Science Letters*, *92*(1), 107–123. doi: http://doi.org/10.1016/0012-821X(89)90025-3

Tanaka, H., Uchida, T., Tanaka, M., Shinohara, H., & Taira, H. (2009). Cosmic-ray muon imaging of magma in a conduit: Degassing process of Satsuma-Iwojima Volcano, Japan. *Geophysical Research Letters*, *36*(1), 1–5. doi: http://doi.org/10.1029/2008GL036451

Townsend, M. (2022). Linking surface deformation to thermal and mechanical magma chamber processes. *Earth and Planetary Science Letters*, *577*,

805 117272. Retrieved from https://doi.org/10.1016/j.epsl.2021.117272
806 doi: 10.1016/j.epsl.2021.117272

807 Turcotte, D., & Schubert, G. (2014). *Geodynamics* (3rd ed.). Cambridge University
808 Press. doi: 10.1017/CBO9780511843877

809 Wessel, B. (2016). *TanDEM-X Ground Segment - DEM Products Specifi-*
810 *cation Document* (Tech. Rep. No. 3.1). Oberpfaffenhofen, Germany:
811 EOC, DLR. Retrieved from https://tandemx-science.dlr.de/ doi:
812 DOI:10.1002/hyp.3360050103

813 Williams-Jones, G., & Rymer, H. (2015). Hazards of Volcanic Gases. In *The ency-*
814 *clopedia of volcanoes* (pp. 985–992). doi: 10.1016/j.jallcom.2009.02.108

815 Wright, R. (2016). MODVOLC: 14 years of autonomous observations of effusive
816 volcanism from space. *Geological Society, London, Special Publications*, *426*,
817 23–53. Retrieved from http://sp.lyellcollection.org/cgi/doi/10.1144/
818 SP426.12 doi: 10.1144/SP426.12

819 Wright, R., Flynn, L. P., Garbeil, H., Harris, A. J. L., & Pilger, E. (2004). MOD-
820 VOLC: Near-real-time thermal monitoring of global volcanism. *Journal of Vol-*
821 *canology and Geothermal Research*, *135*(1-2), 29–49. doi: 10.1016/j.jvolgeores
822 .2003.12.008

823 Yunjun, Z., Fattahi, H., & Amelung, F. (2019). Small baseline InSAR time se-
824 ries analysis: Unwrapping error correction and noise reduction. *Computers and*
825 *Geosciences*, *133*. Retrieved from https://doi.org/10.1016/j.cageo.2019
826 .104331 doi: 10.1016/j.cageo.2019.104331